Energy & Environmental Science

Accepted Manuscript

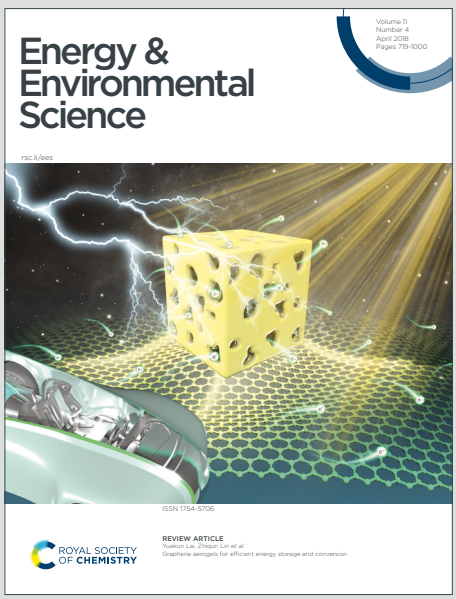

ROYAL SOCIETY OF CHEMISTRY

rsc.li/ees

Boosting Alkaline Hydrogen Evolution: Dominating Role of Interior Modification in Surface Electrocatalysis

Zhao Li[1,2,#], Wenhan Niu[2,#], Zhenzhong Yang[3,#], Abdelkader Kara[4,7], Qi Wang[5], Maoyu Wang[6], Meng Gu[5,], Zhenxing Feng[6,*], Yingge Du[3,*], and Yang Yang[1,2,7,*]*

[1]*Department of Materials Science and Engineering, University of Central Florida, Orlando, FL 32826, United States*

[2]*NanoScience Technology Center, University of Central Florida, Orlando, FL 32826, United States*

[3]*Physical and Computational Sciences Directorate, Pacific Northwest National Laboratory, Richland, Washington 99352, United States*

[4]*Department of Physics, University of Central Florida, Orlando, FL 32826, United States*

[5]*Department of Materials Science and Engineering, Southern University of Science and Technology, Shenzhen 518055, China*

[6]*School of Chemical, Biological, and Environmental Engineering, Oregon State University, Corvallis, OR 97331, United States*

[7]*Energy Conversion and Propulsion Cluster, University of Central Florida, Orlando, FL 32826, United States*

[*]*Email: gum@sustech.edu.cn; zhenxing.feng@oregonstate.edu; Yingge.Du@pnnl.gov; Yang.Yang@ucf.edu;*

[#] *These authors contributed equally to this work.*

TOC

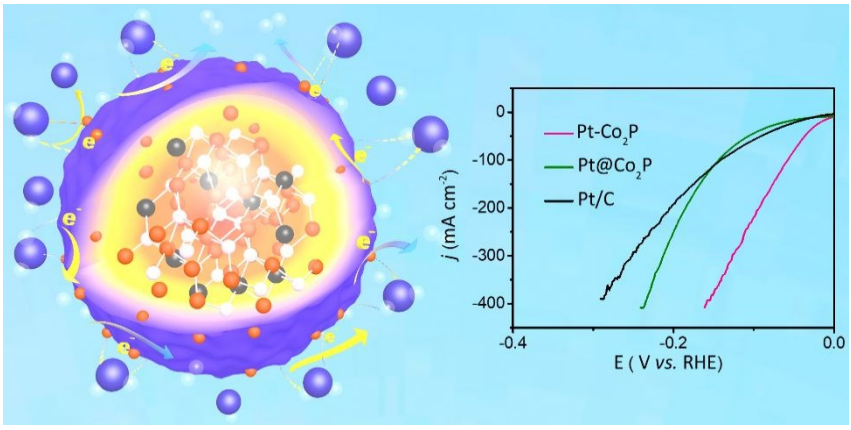

Abstract

Alkaline hydrogen evolution reaction (A-HER) holds great promise for clean hydrogen fuel generation but its practical utilization is severely hindered by the sluggish kinetics for water dissociation in alkaline solutions. Traditional ways to improve the electrochemical kinetics for the A-HER catalysts have been focusing on surface modification, which still can not meet the demanding requirements for practical water electrolysis because of the catalyst surface deactivation. Herein, we report an interior modification strategy to significantly boost A-HER performance. Specifically, a trace amount of Pt was doped in the interior Co_2P (Pt-Co_2P) to introduce stronger dopant-host interaction than the surface-modified catalyst. Consequently, the local chemical state and electronic structure of the catalysts were adjusted to improve the electron mobility and reduce the energy barriers for hydrogen adsorption and H-H bond formation. As a proof-of-concept, the interior-modified Pt-Co_2P shows reduced onset potential at near-zero volt for A-HER, low overpotentials of 2 mV and 58 mV to achieve 10 and 100 mA cm^{-2}, and excellent durability for long-term utilization. The interior-modified Pt-Co_2P delivers superior A-HER performance to Pt/C and the state-of-the-art electrocatalysts. This work will open a new avenue for A-HER catalyst design.

Keywords: interior modification; alkaline hydrogen evolution; water dissociation; near-zero onset potential; dopant-host interaction

1. Introduction

Hydrogen gas (H_2), as a clean alternative fuel to fossil energy, plays crucial roles in developing renewable and sustainable energy future due to its zero-carbon-emission and recyclability.[1-4] Among various H_2 generation techniques, water electrolysis is considered as the most efficient process for high-purity H_2 production.[5] Especially, alkaline hydrogen evolution reaction (A-HER) is of great importance for practical water electrolyzer without concerns about the contamination from the acidic fog and the container corrosion involved in the acidic HER.[6-7] However, extra energy is always required to break the covalent bond in water molecular during A-HER because of the sluggish reaction kinetics for water dissociation.[8] Also, it is very challenging to design catalysts with favorable hydrogen adsorption (hydrogen binding free energy, ΔG_{H^*}) for A-HER.[9] Thus, it is critical to design more efficient A-HER catalysts that can reduce energy barrier and facilitate hydrogen adsorption for H-H bond formation in alkaline electrolyte. So far, platinum (Pt)-based materials are the dominantly used HER catalysts due to the remarkable electronic conductivity, favorable d-band center relative to Fermi energy level, and optimized ΔG_{H^*}.[7, 10-12] However, their natural scarcity and high cost restrict their scalable and practical applications.[13, 14] It is urgent to design emerging catalysts with high A-HER activity and low Pt loading for water electrolysis.

Transition-metal phosphides (TMP) such as cobalt phosphide (Co_2P) have been considered as promising candidates for HER due to their metalloid property and good electrical conductivity, which offer the facilitated catalytic performance in acidic media.[15, 16] However, these TMP catalysts suffer limited HER performance in alkaline solution, owing to the low electron transfer capability and high work function. Hitherto, the most widely applied strategy to improve the A-HER activities of TMP catalysts is through surface modification.[15, 17, 18] For instance, Pt

nanoparticles, clusters, and atoms have been utilized to modify the catalyst surfaces, achieving improved HER activities by the interactions between the surface Pt and TMP catalysts.[1, 9, 19, 20] However, it is still very difficult to overcome additional energy barriers for the adsorbed hydrogen (H*) migration from Pt to TMP on the catalyst surfaces in alkaline solution.[20-22] Moreover, the electrocatalytic activities of the surface-modified catalysts suffer the deactivation issues because of the surface passivation or surface reconstruction during A-HER. Thereupon, it is fundamentally interesting and practically meaningful to answer a question: is it possible to boost the A-HER activity by interior modification of the catalysts?

Herein, we demonstrated a new strategy that directly answered the aforementioned question by contrasting the A-HER performance of surface-modified Co_2P (Pt@Co_2P) and with that of interior-modified Co_2P counterpart (Pt-Co_2P) where Pt was kept to the same trace amount (~3.6 wt%). Especially, the impacts of the catalyst modifications on the reaction pathway, rate-determining step, hydrogen adsorption, and H-H bond formation in alkaline solution were investigated. In contrast to the weak interaction of the surface-modified Pt@Co_2P, the strong interaction between Pt dopant and Co_2P host in the interior-modified Pt-Co_2P efficiently adjusts the local chemical state and electronic structure of Pt-Co_2P, promoting water dissociation, hydrogen adsorption, and H-H bond formation. As a result, Pt-Co_2P exhibits an outstanding A-HER activity with near-zero onset potential and low overpotentials of 2 mV and 58 mV to reach current densities of 10 mA cm^{-2} and 100 mA cm^{-2}, which is superior to the commercial Pt/C and other benchmarking HER catalysts.[23, 24] This work suggests that the interior modification plays a profound role in governing the catalysts' performance even though the reactions occur on the surfaces, which may lead to a new paradigm shift from concentrating on the surface modification for high-performance HER catalyst design.

2. Results and Discussion

The fabrication route for the interior-modified Pt-Co_2P catalyst is illustrated in Figure 1a (more experimental details in Supporting Information). The slightly doped cobalt (Co) by a trace amount of Pt was synthesized by CoPt alloy co-electrodeposition on carbon cloth (CC) followed by thermal phosphorization via chemical vapor deposition (CVD) and surface cleaning via acid. Finally, Pt-Co_2P particles grown on CC were successfully obtained. The interior-modified Pt-Co_2P catalyst uniformly grown on CC is binder-free, of high surface area, and tightly in contact with the current collector, endowing the catalyst with greatly reduced charge transfer resistance across the interfaces.[25] By contrast, the surface-modified Pt@Co_2P was prepared by decorating Co_2P with the electrodeposited Pt nanoparticles. The Pt contents in both Pt-Co_2P and Pt@Co_2P catalysts were measured to be 3.6 wt% by X-ray fluorescence and inductively coupled plasma mass spectroscopy (XRF and ICP-MS, Table S1).

Crystal structures of Co_2P, Pt@Co_2P, and Pt-Co_2P were characterized by X-ray diffraction (XRD, Figure 1b). The characteristic peaks at 40.76°, 43.17°, 50.41°, and 52.05°, marked by asterisks, corresponding to (121), (211), (310), and (131) planes, respectively, match well with Co_2P (JCPDS No. 32-0306), indicating the same main crystalline phase of the catalysts. Meanwhile, no diffraction peak of Pt, especially the characteristic peak located around at 39.60° for Pt (111), can be identified in the catalysts, confirming the low content of Pt doping.[14, 26, 27] The shifted diffraction peaks of Pt-Co_2P (Figure S1) suggest the lattice distortion induced by the incorporation of Pt dopants in the crystal structure of Co_2P, which contribute to the enhanced catalytic activity.[14]

Scanning electron microscopy (SEM) and transmission electron microscopy (TEM) images (Figure 1c-d) show that Pt-Co_2P particles with a size distribution from 125 nm to 150 nm uniformly

grow on carbon cloth (CC). The high-angle annular dark-field scanning TEM images (HAADF-STEM, Figure 1e) confirm that 7-10 nm thin layer was uniformly covered on the surface of Pt-Co_2P particles. The corresponding energy dispersive spectroscopy (EDS) line scan reveals a higher P-content on the surface of Pt-Co_2P (Figure f). The catalysts with P-rich surfaces are favorable for enhancing the interaction between the surface active sites with water molecules and thus help to break the H-OH bond.[28] The low content of Pt uniformly distributed across Pt-Co_2P as compared to those of Co and P further confirms the successful incorporation of a trace amount of Pt in the interior Co_2P. The interior Pt dopants play an important role in modulating the local electronic structure of Co_2P, which consequently contributes to forming favorable thermo-neutral active sites for HER.[29] The element composition and distribution of Pt-Co_2P were analyzed by the STEM-EDS mapping (Figure 1g-j), where Pt, Co, and P were uniformly distributed in the Pt-Co_2P particles. Specifically, the high intensity of the P signal is localized on the outmost layer of Pt-Co_2P particles. To further characterize the crystal phase and composition of Pt-Co_2P particles, the TEM images and the corresponding fast Fourier transformation (FFT) were analyzed in Figure 1k-o. As shown in the TEM images (Figure 1k-l), the outmost region can be clearly distinguished from the bulk as marked by the yellow dash lines. Meanwhile, the selected areas 1-4 were recorded by blue and white dash squares in Figure 1l. The FFT patterns (Figure 1m) in the blue dash area suggest that the outmost regions have two sets of lattice spacings (1.78 Å and 2.03 Å; 2.18 Å and 2.02 Å), corresponding to (311) and (310); (121) and (310) facets of Co_2P, respectively. The high-resolution TEM (HRTEM) images in Figure 1n further reveal the disordered lattice structures observed in the outmost region, suggesting imperfect crystallization caused by the defects formed in the P-rich surface layer.[2] The interior Pt-Co_2P identified by the FFT pattern (Figure 1m) shows that the lattice spacings (3.20 Å and 1.79Å) belonging to (101) and (002) facets of Co_2P, slightly

increased as compared to the standard Co_2P because of the Pt doping effect. Meanwhile, atomic-resolution images illustrated in Figure S2 reveals no obvious Pt clusters grown in Pt-Co_2P. All the above evidence strongly proves that Pt has been uniformly doped into our Pt-Co_2P catalyst. In addition, Pt@Co_2P was also characterized as shown in Figure S3. Different from Pt-Co_2P, the TEM image of Pt@Co_2P (Figure S3a-b) shows that Pt nanoparticles (~5 nm) uniformly anchor on the surface of Co_2P. The EDS element mapping confirms the coexistence of Co, P, and Pt in Pt@Co_2P with concentrated Pt in the outmost layer, further verifying that Pt nanoparticles are decorated on the surface of Co_2P (Figure S3c-f).

To have an insightful understanding of the structure-property relationship of the designed A-HER catalysts, X-ray photoelectron spectroscopy (XPS) and X-ray absorption spectroscopy (XAS) including the X-ray absorption near-edge structure (XANES) and extended X-ray absorption fine structure (EXAFS) were employed to study the impacts of the catalyst (surface or interior) modification methods on the chemical states, local bonding, electronic structures, and compositions of Pt-Co_2P, Pt@Co_2P, and Co_2P. The high-resolution XPS spectra confirm the existence of Pt, Co, and P in the catalysts (Figure 2a-c). The XPS Pt peaks (Figure 2a) for Pt-Co_2P located at 71.12 eV and 74.84 eV are assigned to metallic Pt (0). Two XPS peaks at 72.33 eV and 75.61 eV are ascribed to the $4f_{7/2}$ and $4f_{5/2}$ of Pt (2+).[30] It also suggests that Pt-Co_2P has a higher atomic ratio of Pt^{2+}/Pt^0 (0.4, Table S2) than that of Pt@Co_2P (0.24), indicating a stronger electronic interaction between Pt atoms and Co_2P for regulating hydrogen evolution.[31] The high-resolution XPS Co $2p_{3/2}$ peaks (Figure 2b) for Pt-Co_2P located at 778.79 eV and 780.91 eV are assigned to the Co-P bond in Co_2P.[32] Furthermore, the Co^{2+}/Co^{3+} ratio estimated by fitting XPS Co $2p_{3/2}$ peaks for Pt-Co_2P is higher than that for Pt@Co_2P (Table S3), further confirming a stronger electronic interaction in the interior-modified Pt-Co_2P than the surface-modified Pt@Co_2P.[33-35] The high-

resolution XPS P 2p peaks (Figure 2c) located at 129.45 eV and 130.36 eV correspond to P $2p_{3/2}$ and P $2p_{1/2}$ for the negatively charged P (Co-P bond) in Co_2P.[36, 37] An isolated peak at 133.14 eV indicates the naturally oxidized P on the catalyst surface, which has been reported in many TMP catalysts.[38-40]

Ultraviolet photoelectron spectroscopy (UPS, Figure 2d) was used to explore the impacts of modification methods (Pt on the surface or in the interior of Co_2P) on the energy levels of Pt-Co_2P, Pt@Co_2P, and Co_2P, which were estimated to be 7.07 eV, 7.35 eV, and 7.47 eV, respectively, by subtracting 21.22 eV of He I UPS spectra. The lower energy level of Pt-Co_2P indicates higher electron mobility for hydrogen generation than Pt@Co_2P and Co_2P.[41] Moreover, the Pt dopants in the Pt-Co_2P catalyst can modulate the local electronic structure and the chemical state of Co_2P, thus resulting in considerable active sites and delicate ΔG_{H^*} for efficient A-HER.

To understand the oxidization state and corresponding local structure of our catalysts, the X-ray absorption spectroscopy (XAS),[42-44] including X-ray absorption near-edge structure (XANES) and extended X-ray absorption fine structure (EXAFS) were performed and shown in Figure 2e-2f. The corresponding XANES edge of Pt-Co_2P shifts to higher energy compared to Pt@Co_2P and Pt. It suggests a higher oxidation state of Pt in Pt-Co_2P, agreeing well with the results from XPS analysis. For EXAFS, the peak around 2.1Å in Pt-Co_2P is shorter than the Pt-Pt metal peak (2.5Å) in Pt metal, which could be treated as Pt-P peak or Pt-Co peak. To further verify the local coordination structure of Pt, we used the structure model generated from theoretical calculation to fit the EXAFS spectrum of Pt-Co_2P. The analysis (Figure S4 and Table S4) shows the co-existence of Pt-P and Pt-Co bonds, which confirms that Pt doped into the Co_2P matrix with P. The higher amplitude of Pt-P and Pt-Co in the EXAFS of Pt-Co_2P than that of Pt@Co_2P also indicates the stronger dopant-host interaction in Pt-Co_2P. Consequently, the local electronic structure of Pt-

Co_2P can be effectively modified by the regulation of energy levels as illustrated in UPS (Figure 2d). It is favorable for the enhancement of electron mobility and reducing the energy barriers for A-HER with high efficiency.

To further study the structure-property relationship of the catalysts, the A-HER performance of Pt-Co_2P, Pt@Co_2P, and control samples such as Co_2P and Pt/C were examined in a typical three-electrode cell in alkaline solution (Figure 3a-c). All the polarization curves were treated with iR-compensation. The reference electrode was calibrated in a high purity H_2-saturated electrolyte (Figure S5). Linear sweep voltammetry (LSV) curves (Figure 1a and Figure S6) show that Co_2P exhibits an inferior A-HER performance (e.g. larger overpotentials at different current densities) among all the catalysts. Both surface-modified Pt@Co_2P and interior-modified Pt-Co_2P show significantly improved A-HER performance by introducing a trace amount of Pt to Co_2P. Especially, Pt-Co_2P delivers a much lower overpotential of 2 mV to achieve 10 mA cm^{-2} than those of Pt@Co_2P (19 mV), commercial Pt/C (20 mV), and the state-of-the-art HER catalysts (Table S5). It should be noted that the overpotentials of Pt-Co_2P are still prominently lower than those of Pt@Co_2P and Pt/C at increased current densities, indicating an improved H_2 bubble release and favorable reactant adsorption.[45] We also tested the repeatability of Pt-Co_2P for A-HER (Figure S7) using three Pt-Co_2P catalysts fabricated from different batches, showing almost consistent A-HER activities and the excellent reproducibility of Pt-Co_2P. The electrocatalytic A-HER performance tested by LSV directly validates our hypothesis that the interior-modified Pt-Co_2P prepared by introducing Pt species into the interior Co_2P could efficiently improve the A-HER activity of Co_2P as compared to the surface-modified Pt@Co_2P and Pt/C. The PtCo alloy (Figure S8-10) was further examined to verify the interior modification as a general approach in regulating the A-HER performance. Moreover, the Tafel slopes were analyzed to have insights into the reaction kinetics

for A-HER. The Tafel slope (Figure 3c) for Pt@Co_2P was estimated to be 119 mV dec^{-1}, indicating that the A-HER is dominated by the Volumer step due to the sluggish kinetics for water dissociation.[41] However, Pt-Co_2P shows a much smaller Tafel slope of 44 mV dec^{-1} than those of Pt@Co_2P and commercial Pt/C (65 mV dec^{-1}), suggesting a favorable Volumer-Heyrosky pathway and facilitated electron transfer kinetics for A-HER.

The mass activity and electrochemical active surface area (ECSA) were also evaluated to provide an insightful understanding of the intrinsic activities of the catalysts. As shown in Figure 3d, Pt-Co_2P delivers a higher mass activity than Pt@Co_2P and Pt/C at different overpotentials, strongly supporting our hypothesis that the interior modification of Co_2P is more efficient than the traditional surface modification.[46] Furthermore, the ECSA was estimated by calculating the double-layer capacitance (C_{dl}, Figure 3e).[47, 48] The C_{dl} of Pt-Co_2P (26.48 mF cm^{-2}) is higher than those of Pt@Co_2P (21.77 mF cm^{-2}) and Co_2P (13.38 mF cm^{-2}, Figure S11), indicating that the Pt doping in the interior Co_2P increase the ECSA and overall active sites. It is another direct evidence proving our concept that the Pt dopants incorporated in the interior Co_2P strongly interacts with surrounding Co and P, leading to greatly increased surface active sites for A-HER.

To further understand the drastically improved A-HER performance of Pt-Co_2P through the interior Pt doping, more solid pieces of evidence were demonstrated in Figure S12-15. First of all, the underpotential deposition (UPD) method was adopted to evaluate the density of active sites.[49] The CV curves of Pt-Co_2P and Pt@Co_2P in Figure S12 demonstrate the signal of underpotential Cu tripping corresponding to the number of active sites for the catalytic reactions. The stronger intensity of the underpotential Cu tripping for Pt-Co_2P emblematizes the increased number of active sites when compared with that for Pt@Co_2P.[3, 50] Precisely, the density of the active sites was calculated to be 1.02×10^{18} sites cm^{-2} for Pt-Co_2P, greater than that of Pt@Co_2P (7.45×10^{17}

sites cm^{-2}, Figure S13). Besides, the turnover frequency (TOF) for Pt-Co_2P is greater than that of Pt@Co_2P at the same overpotential (Figure S14). To built a relationship of the Tafel plots with TOF, the exchange current measured from Figure 3c was further employed to evaluate the value of TOF for Pt-Co_2P with 0.031 s^{-1}, outperforming that of Pt@Co_2P (0.026 s^{-1}).[51] Furthermore, to evaluate the intrinsic activity of our catalysts, the quantitative characterizations of the electrocatalytic activities, including LSV curves, Tafel slope, mass activity, and TOF, were normalized by ECSA (Figure S15). The electrochemical activities of Pt-Co_2P are superior to Pt@Co_2P, proving its remarkably intrinsic activity. To validate the importance of interior Pt dopant in Pt-Co_2P, full range of CV curves were recorded in Figure S16. No characteristic Pt-based H/OH adsorption and desorption peaks can be detected from Pt-Co_2P in alkaline and acid electrolyte. It reveals that Pt in Pt-Co_2P is not the primarily exposed surface active site. From another perspective, it indirectly highlights the significance of incorporation of interior Pt dopant in the regulation of the electronic structure of Co_2P and consequently the promotion of overall catalytic performance of Pt-Co_2P.

The A-HER stabilities for the catalysts were galvanostatically examined in a two-electrode set-up with a carbon rod as the counter electrode in 1 M KOH for overall water splitting (Figure 3f). Pt-Co_2P can keep the potential at the current density of 100 mA cm^{-2} for 200 hours. However, unfortunately, Pt@Co_2P and Pt/C show poor stabilities during the long-term testing, which is mainly due to the catalyst deactivation in extreme alkaline solution. In addition, we also examined the galvanostatic stabilities of Pt-Co_2P as compared to commercial Pt/C at different current densities from 1 mA cm^{-2} to 100 mA cm^{-2}. With increasing the current density, the required potential for overall water splitting increases gradually. Meanwhile, Pt-Co_2P exhibits better reversibility and durability than Pt/C when decreasing the current density. Furthermore, to verify

our catalyst as a favorite electrode during long stability test, both high-resolution TEM images and EXAFS of Pt L-edge corresponding to Pt-Co_2P were recorded after the stability test as shown in Figure S17-18. It gives close results to that before the stability test, suggesting almost negligible structural changes. Moreover, with model-based analysis (Table S6), we could not find any change of coordination number for all related Pt-P and Pt-Co bonds, suggesting the robustness of Pt-Co_2P realized by interior modification.

Moreover, the density of functional theory (DFT) simulations were used to understand the catalytic mechanism of Pt-Co_2P (more calculation details in Supporting Information). The atomic structure models build up with and without the incorporation of Pt dopant, whose presence could alter the local atomic and electronic structure of Co_2P. Firstly, the partial densities of states (PDOS, Figure 4a) were evaluated to understand the role of Pt doping in the improved intrinsic A-HER activity. The calculation results suggest that Pt dopant can greatly impact the electronic states of Pt-Co_2P, consistent with XPS and UPS results. Specifically, the PDOS near the Fermi level is greatly enhanced as a result of the dopant-host interaction.[52] Note that the efficient changes in Co PDOS reveal its dominant role in the enhanced catalytic activity. Moreover, the DFT calculations were further employed to understand how the components inside Pt-Co_2P cooperate synergistically to activate the A-HER. It is worth highlighting that we replaced 8 (out of 16) Co surface atoms by P atoms, reaching a 50/50 stoichiometry to mimic the surface P-rich Co_2P (denoted as S-Co_2P), trying to correlate well with the results from STEM-EDS and XPS (Figure 1e-f and Figure 2b-c). Figure 4b records the energy diagrams of A-HER for Pt-Co_2P, S-Co_2P, and Co_2P. In comparison with Co_2P, the lower energy barriers for Pt-Co_2P and S-Co_2P confirm the role of phosphor in accelerating water dissociation. Moreover, the adsorption of H and OH were calculated at different adsorption sites. We found that H and OH prefer binding to Co atoms revealing that Co atoms as

the main active sites for A-HER. Overall, the difference in total energy between the case where both H and OH are adsorbed on the surface, and the case where H is adsorbed and OH released from the surface of Pt-Co_2P is lowest (0.49 eV). Furthermore, the energy as shown in Figure 4c suggests a preferred A-HER for Pt-Co_2P as compared to S-Co_2P and Co_2P. All the above evidence proves that Pt dopant can regulate the hydrogen adsorption and H-H bond formation for the enhanced A-HER following the Volmer-Heyrovsky mechanism.

Electrochemical impedance spectroscopy (EIS) was further carried out to exploit the charge transfer kinetics for the electrochemical processes involved in A-HER, including hydrogen adsorption and H-H bond formation.[53] As shown in Figure S19, a smaller charge transfer resistance (R_1) for Pt-Co_2P than Pt@Co_2P was observed, suggesting an enhanced electronic conductivity and accelerated reaction kinetics. Note that the hydrogen adsorption resistance (R_2) and the corresponding pseudo-capacitances (C_φ) can be estimated by EIS. As demonstrated in Figure S20-21, the R_2 for Pt-Co_2P is overpotential-dependent and smaller than that for Pt@Co_2P, revealing the improved hydrogen adsorption resulting from the strong electronic interaction between Pt dopant and Co_2P host. Furthermore, the hydrogen coverage estimated by the C_φ as a function of overpotential (Figure 4d) was used as indirect evidence for hydrogen adsorption on the catalyst surface. The integral area of Pt-Co_2P (hydrogen adsorption charge) is larger than that of Pt@Co_2P, suggesting the increased hydrogen adsorption as a result of the favorable water dissociation. As shown in the EIS-Tafel plots (Figure 4e), Pt-Co_2P shows higher activity than Pt@Co_2P, further confirming the regulated hydrogen adsorption and H-H bond formation for the enhanced A-HER.[53]

A possible mechanism for the improved A-HER activity of Co_2P by the interior modification using a trace amount of Pt is illustrated in Figure 4f. The overall A-HER process for both Pt-Co_2P and Pt@Co_2P follows the Volumer-Heyrosky pathway, however, they are dominated by different

rate-determining steps. For Pt-Co_2P (left schematic in Figure 4f), the Pt doping in the interior Co_2P can optimize the electronic structure of the catalyst. The P-rich surface is favorable for water dissociation as explained in DFT calculation (Figure 4b). Because of the modified electronic structure, H* could be easily formed and converted to H_2 through the Heyrovsky step on the active Co sites, which is the rate-determining step for Pt-Co_2P. Whereas the rate-determining step for the surface-modified Pt@Co_2P (right schematic in Figure 4f) is dominated by the Volumer step due to the insufficiently optimized local electronic structure.

A series of catalysts, including Pt-$Ni_{2.25}P$, Pt-ZnP_4, and Pt-WP, were synthesized using the proposed interior-modification strategy (Figure S22) to further verify the versatility of the technique. In comparison with our Pt-Co_2P, they possess distinguished HER performance as well, proving that our design conception can be considered as a universal strategy in designing novel catalysts. It will open a new avenue for clean energy conversion and storage applications.

3. Conclusion

In summary, a new strategy for modulating the local electronic structure of the catalyst for A-HER by interior modification was designed. The interior-modified Pt-Co_2P provides an adjusted electronic structure, which is favorable for water dissociation and hydrogen evolution. Specifically, the Pt doping in the interior Co_2P reduces the energy barriers for hydrogen adsorption and H-H bond formation. As a proof-of-concept, Pt-Co_2P possesses a near-zero onset potential for A-HER and lower overpotentials of 5 mV and 58 mV to achieve 10 mA cm^{-2} and 100 mA cm^{-2}, respectively. Besides, the unique Pt-Co_2P catalyst with excellent electrochemical durability and reversibility is favorable for overall water splitting. This work provides a new paradigm for the rational design of efficient catalysts for A-HER.

Supporting Information

The Supporting Information is available free of charge on the Publications website. Materials and electrochemical characterizations.

Acknowledgments

This work was supported by the National Science Foundation under Grant No. CMMI-1851674 and the startup grant from the University of Central Florida. The XPS test was supported by the NSF MRI XPS: ECCS: 1726636, hosted in MCF-AMPAC facility, MSE, CECS, UCF. TEM and data analysis were supported by the U.S. Department of Energy, Office of Science, Office of Basic Energy Sciences, Early Career Research Program under award # 68278. A portion of the research was performed using EMSL, a DOE User Facility sponsored by the Office of Biological and Environmental Research and located at the Pacific Northwest National Laboratory. Part of the microscopy work was supported by the National Natural Science Foundation of China (No. 21802065). The computational work of AK is supported by the U.S. Department of Energy Basic Energy Science under Contract No DE-FG02-11ER16243. Resources of the National Energy Research Scientific Computing Center (NERSC) were used fort he computational part of this paper. This research used resources of the beamline 5-BM-D, of DND-CAT at the Advanced Photon Source (APS), a U.S. Department of Energy (DOE) Office of Science User Facility operated for the DOE Office of Science by Argonne National Laboratory under Contract DE-AC02-06CH11357. DND-CAT is supported through E. I. duPont de Nemours & Co., Northwestern University, and The Dow Chemical Company.

References

1. H. Zhang, P. An, W. Zhou, B. Y. Guan, P. Zhang, J. Dong and X. W. D. Lou, *Sci. Adv.*, 2018, **4**, eaao6657.
2. Z. Li, W. Niu, L. Zhou and Y. Yang, *ACS Energy Lett.*, 2018, **3**, 892-898.
3. X. Zhang, Z. Luo, P. Yu, Y. Cai, Y. Du, D. Wu, S. Gao, C. Tan, Z. Li, M. Ren, T. Osipowicz, S. Chen, Z. Jiang, J. Li, Y. Huang, J. Yang, Y. Chen, C. Y. Ang, Y. Zhao, P. Wang, L. Song, X. Wu, Z. Liu, A. Borgna and H. Zhang, *Nat. Catal.*, 2018, **1**, 460-468.
4. J. Yuanyuan, D. Kai, L. Yizhong, L. Jiawei, C. Bo, S. Zhongqian and N. Li, *Sci. China Mater.,* 2020, DOI: 10.1007/s40843-020-1282-6.
5. X. Zou and Y. Zhang, *Chem. Soc. Rev.*, 2015, **44**, 5148-5180.
6. N. Mahmood, Y. Yao, J. W. Zhang, L. Pan, X. Zhang and J. J. Zou, *Adv. Sci*, 2018, **5**, 1700464.
7. Z. F. Huang, J. Song, K. Li, M. Tahir, Y. T. Wang, L. Pan, L. Wang, X. Zhang and J. J. Zou, *J. Am. Chem. Soc.*, 2016, **138**, 1359-1365.
8. J. X. Feng, J. Q. Wu, Y. X. Tong and G. R. Li, *J. Am. Chem. Soc.*, 2018, **140**, 610-617.
9. J. Park, S. Lee, H.-E. Kim, A. Cho, S. Kim, Y. Ye, J. W. Han, H. Lee, J. H. Jang and J. Lee, *Angew. Chem. Int. Ed. Engl.*, 2019, **131,** 16184-16188.
10. Z. W. Seh, J. Kibsgaard, C. F. Dickens, I. Chorkendorff, J. K. Norskov and T. F. Jaramillo, *Science*, 2017, **355**.
11. B. Chen, G. Sun, J. Wang, G. Liu, C. Tan, Y. Chen, H. Cheng, J. Chen, Q. Ma and L. Huang, *ChemComm*, 2020. DOI: 10.1039/D0CC00506A.
12. Z. Zhang, G. Liu, X. Cui, B. Chen, Y. Zhu, Y. Gong, F. Saleem, S. Xi, Y. Du and A. Borgna, *Adv. Mater.*, 2018, **30**, 1801741.
13. G. Wang, Z. Yang, Y. Du and Y. Yang, *Angew. Chem. Int. Ed. Engl.*, 2019, **131**, 15995-16001.
14. Z. Li, W. Niu, Z. Yang, N. Zaman, W. Samarakoon, M. Wang, A. Kara, M. Lucero, M. V. Vyas and H. Cao, *Energy Environ. Sci.*, 2020, **13**, 884-895.
15. C. Tang, L. Gan, R. Zhang, W. Lu, X. Jiang, A. M. Asiri, X. Sun, J. Wang and L. Chen, *Nano Lett.*, 2016, **16**, 6617-6621.
16. J. Tian, Q. Liu, N. Cheng, A. M. Asiri and X. Sun, *Angew. Chem. Int. Ed. Engl.*, 2014, **53**, 9577-9581.
17. K. Xu, H. Cheng, H. Lv, J. Wang, L. Liu, S. Liu, X. Wu, W. Chu, C. Wu and Y. Xie, *Adv.*

Mater., 2018, **30**. 1703344.

18. K. Xu, H. Ding, M. Zhang, M. Chen, Z. Hao, L. Zhang, C. Wu and Y. Xie, *Adv Mater*, 2017, **29**, 1606980.
19. Z. Wang, X. Ren, Y. Luo, L. Wang, G. Cui, F. Xie, H. Wang, Y. Xie and X. Sun, *Nanoscale*, 2018, **10**, 12302-12307.
20. J. Li, H.-X. Liu, W. Gou, M. Zhang, Z. Xia, S. Zhang, C.-R. Chang, Y. Ma and Y. Qu, *Energy Environ. Sci.*, 2019, **12**, 2298-2304.
21. C. Tang, R. Zhang, W. Lu, L. He, X. Jiang, A. M. Asiri and X. Sun, *Adv. Mater.*, 2017, **29**. 1602441.
22. M. Choi, S. Yook and H. Kim, *ChemCatChem*, 2015, **7**, 1048-1057.
23. P. Xiao, W. Chen and X. Wang, *Adv. Energy Mater.*, 2015, **5**, 1500985.
24. G. Zhao, K. Rui, S. X. Dou and W. Sun, *Adv. Funct. Mater.*, 2018, **28**, 1803291.
25. K. Liang, L. Li and Y. Yang, *ACS Energy Lett.*, 2017, **2**, 373-390.
26. J. Jones, H. Xiong, A. T. DeLaRiva, E. J. Peterson, H. Pham, S. R. Challa, G. Qi, S. Oh, M. H. Wiebenga and X. I. P. Hernández, *Science*, 2016, **353**, 150-154.
27. M. A. Shah, *Sci. Iran.*, 2012, **19**, 964-966.
28. R. Zhang, X. Wang, S. Yu, T. Wen, X. Zhu, F. Yang, X. Sun, X. Wang and W. Hu, *Adv. Mater.*, 2017, **29**. 1605502.
29. M. Lao, K. Rui, G. Zhao, P. Cui, X. Zheng, S. X. Dou and W. Sun, *Angew. Chem. Int. Ed. Engl.*, 2019, **58**, 5432-5437.
30. J. Zhu, G. He and P. K. Shen, *J. Power Sources*, 2015, **275**, 279-283.
31. M. Lao, K. Rui, G. Zhao, P. Cui, X. Zheng, S. X. Dou and W. Sun, *Angew. Chem. Int. Ed. Engl.*, 2019, **58**, 5432-5437.
32. A. Dutta, A. K. Samantara, S. K. Dutta, B. K. Jena and N. Pradhan, *ACS Energy Lett.*, 2016, **1**, 169-174.
33. S. A. Makhlouf, M. A. Kassem and M. A. Abdel-Rahim, *J. Mater. Sci.*, 2009, **44**, 3438-3444.
34. J. Zhang, X. Wu, W. C. Cheong, W. Chen, R. Lin, J. Li, L. Zheng, W. Yan, L. Gu, C. Chen, Q. Peng, D. Wang and Y. Li, *Nat. Commun.*, 2018, **9**, 1002.
35. H. Wu, G. Wu, Y. Ren, L. Yang, L. Wang and X. Li, *J. Mater. Chem. C*, 2015, **3**, 7677-7690.
36. J. Song, C. Zhu, B. Z. Xu, S. Fu, M. H. Engelhard, R. Ye, D. Du, S. P. Beckman and Y.

Lin, *Adv. Energy Mater.*, 2017, **7**, 1601555.

37. Z. Huang, Z. Chen, Z. Chen, C. Lv, M. G. Humphrey and C. Zhang, *Nano Energy*, 2014, **9**, 373-382.
38. Q. Gao, W. Zhang, Z. Shi, L. Yang and Y. Tang, *Adv. Mater.*, 2019, **31**, e1802880.
39. K. Liang, S. Pakhira, Z. Yang, A. Nijamudheen, L. Ju, M. Wang, C. I. Aguirre-Velez, G. E. Sterbinsky, Y. Du, Z. Feng, J. L. Mendoza-Cortes and Y. Yang, *ACS Catal.*, 2019, **9**, 651-659.
40. Y. Yang, H. Fei, G. Ruan and J. M. Tour, *Adv. Mater.*, 2015, **27**, 3175-3180.
41. Y. Shi, Y. Zhou, D. R. Yang, W. X. Xu, C. Wang, F. B. Wang, J. J. Xu, X. H. Xia and H. Y. Chen, *J. Am. Chem. Soc.*, 2017, **139**, 15479-15485.
42. M. Wang, L. Árnadóttir, Z. J. Xu and Z. Feng, *Nano-Micro Lett.*, 2019, **11**, 47.
43. M. Wang, B. Han, J. Deng, Y. Jiang, M. Zhou, M. Lucero, Y. Wang, Y. Chen, Z. Yang, A. T. N'Diaye, Q. Wang, Z. J. Xu and Z. Feng, *ACS Appl. Mater. Interfaces*, 2019, **11**, 5682-5686.
44. Z. Feng, Q. Ma, J. Lu, H. Feng, J. W. Elam, P. C. Stair and M. J. Bedzyk, *RSC Adv.*, 2015, **5**, 103834-103840.
45. J. X. Feng, S. Y. Tong, Y. X. Tong and G. R. Li, *J. Am. Chem. Soc.*, 2018, **140**, 5118-5126.
46. Y. Cheng, S. Lu, F. Liao, L. Liu, Y. Li and M. Shao, *Adv. Funct. Mater.*, 2017, **27**, 1700359.
47. J. X. Feng, H. Xu, Y. T. Dong, X. F. Lu, Y. X. Tong and G. R. Li, *Angew. Chem. Int. Ed. Engl.*, 2017, **56**, 2960-2964.
48. T. Liu, P. Li, N. Yao, G. Cheng, S. Chen, W. Luo and Y. Yin, *Angew. Chem. Int. Ed. Engl.*, 2019, **58**, 4679-4684.
49. C. L. Green and A. Kucernak, *J. Phys. Chem. B*, 2002, **106**, 1036-1047.
50. X. Yang, A.-Y. Lu, Y. Zhu, M. N. Hedhili, S. Min, K.-W. Huang, Y. Han and L.-J. Li, *Nano Energy*, 2015, **15**, 634-641.
51. D. Voiry, H. Yamaguchi, J. Li, R. Silva, D. C. Alves, T. Fujita, M. Chen, T. Asefa, V. B. Shenoy and G. Eda, *Nat. Mater.*, 2013, **12**, 850-855.
52. K. Jiang, B. Liu, M. Luo, S. Ning, M. Peng, Y. Zhao, Y. R. Lu, T. S. Chan, F. M. F. de Groot and Y. Tan, *Nat. Commun.*, 2019, **10**, 1743.
53. A. Damian and S. Omanovic, *J. Power Sources*, 2006, **158**, 464-476.

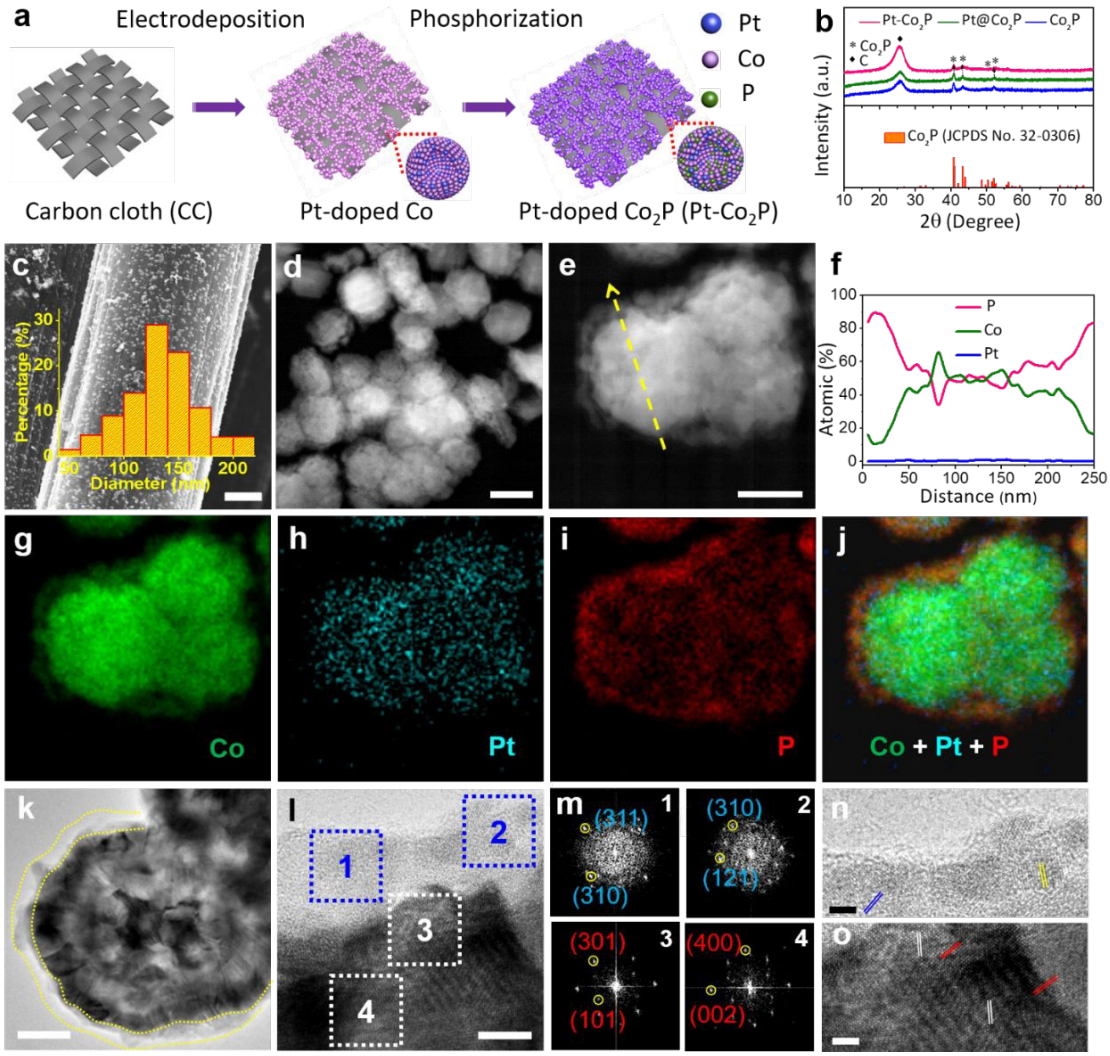

Figure 1. (a) Schematic illustration of the fabrication process of Pt-Co_2P. (b) XRD patterns of Pt-Co_2P, Pt@Co_2P, and Co_2P supported on CC. (c) SEM images of Pt-Co_2P particles grown on CC. The inset is the particle size distribution. Scale bar: 2 μm. (d, e) HAADF-STEM images of Pt-Co_2P. Scale bars: 200 nm and 100 nm, respectively. (f-j) EDS line scan and STEM-EDS elemental mapping. (k-l) High-resolution TEM images of Pt-Co_2P. Scale bars: 50 nm and 5 nm, respectively. (m) FFT patterns selected from the blue and white dash zones in (l), where zones 1-2 and 3-4 represent the P-rich surface and well-crystallized interior Co_2P, respectively. (n-o) Lattice spacings

of Pt-Co_2P. Scale bar: 2 nm. Note that blue, yellow, red, and white lines represent Co_2P (311), (121), (301), and (002) planes, respectively.

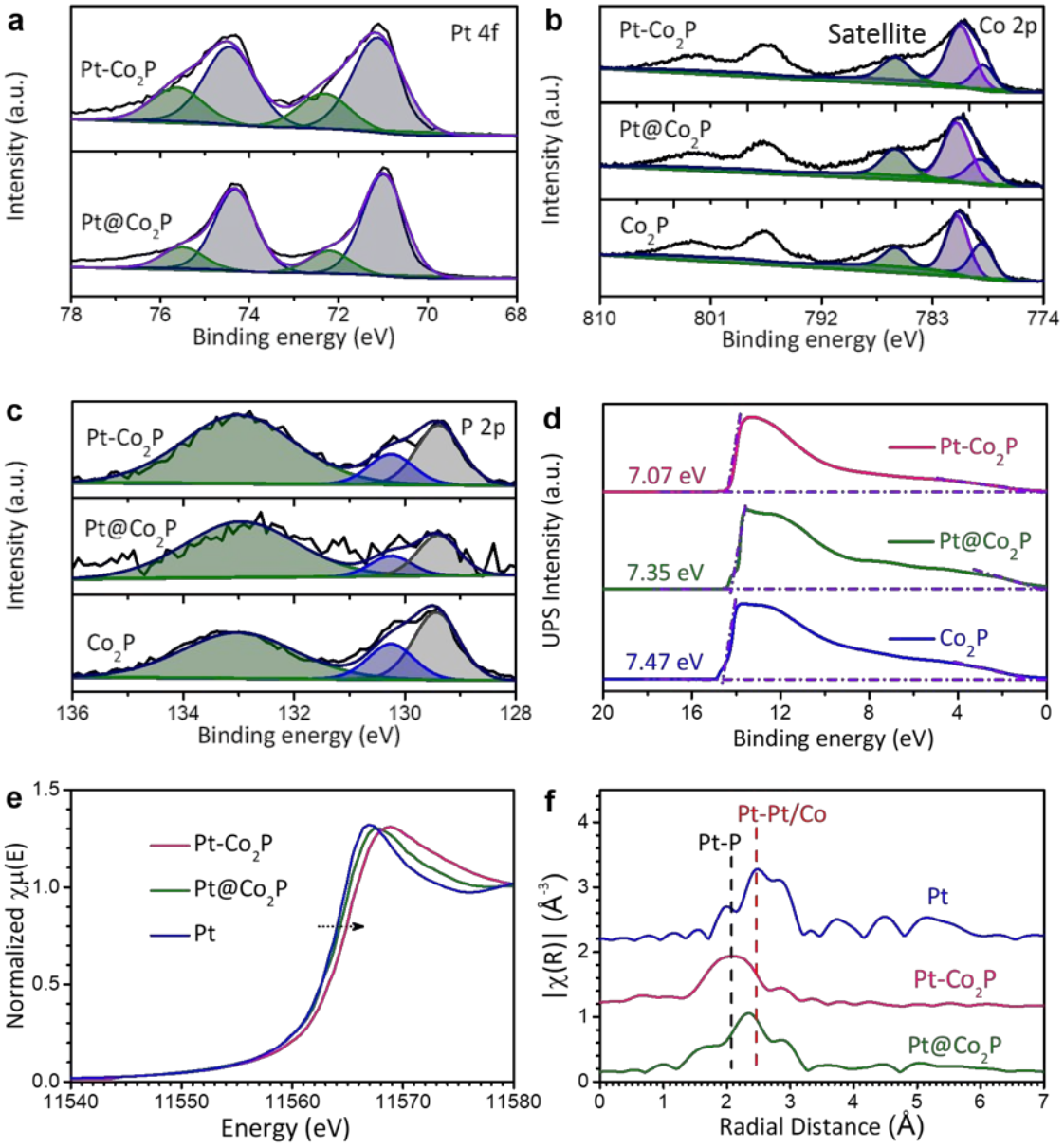

Figure 2. Spectral investigation of the catalysts by XPS and UPS. The high-resolution XPS spectra of (a) Pt 4f, (b) Co 2p, and (c) P 2p. (d) UPS spectra of the catalysts. The Pt L-edge (e) XANES, and (f) EXAFS spectra of Pt, Pt-Co_2P, and Pt@Co_2P, respectively.

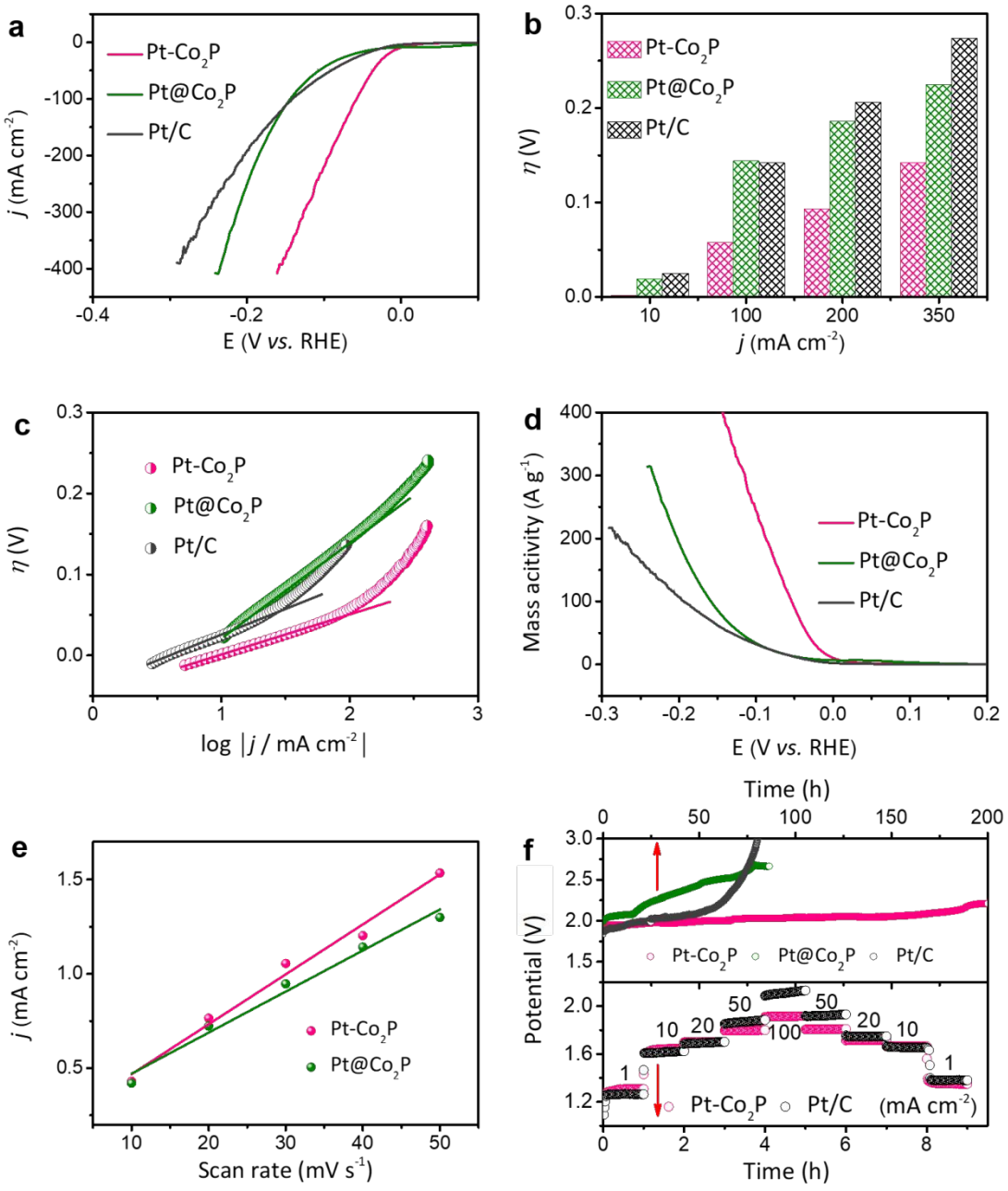

Figure 3. A-HER performance of the catalysts in 1 M KOH. (a) LSV curves of the catalysts tested at 5 mV s^{-1}. (b) The overpotentials required to achieve different current densities (10, 100, 200, and 350 mA cm^{-2}). (c) Tafel plots. (d) Mass activities at different overpotentials. (e) The ECSA of Pt-Co_2P and Pt@Co_2P. (f) The stability at 100 mA cm^{-2} and overall water splitting performance of the catalysts at different current densities (1, 10, 20, 50, and 100 mA cm^{-2}) in a two-electrode set-up with a carbon rod as the counter electrode.

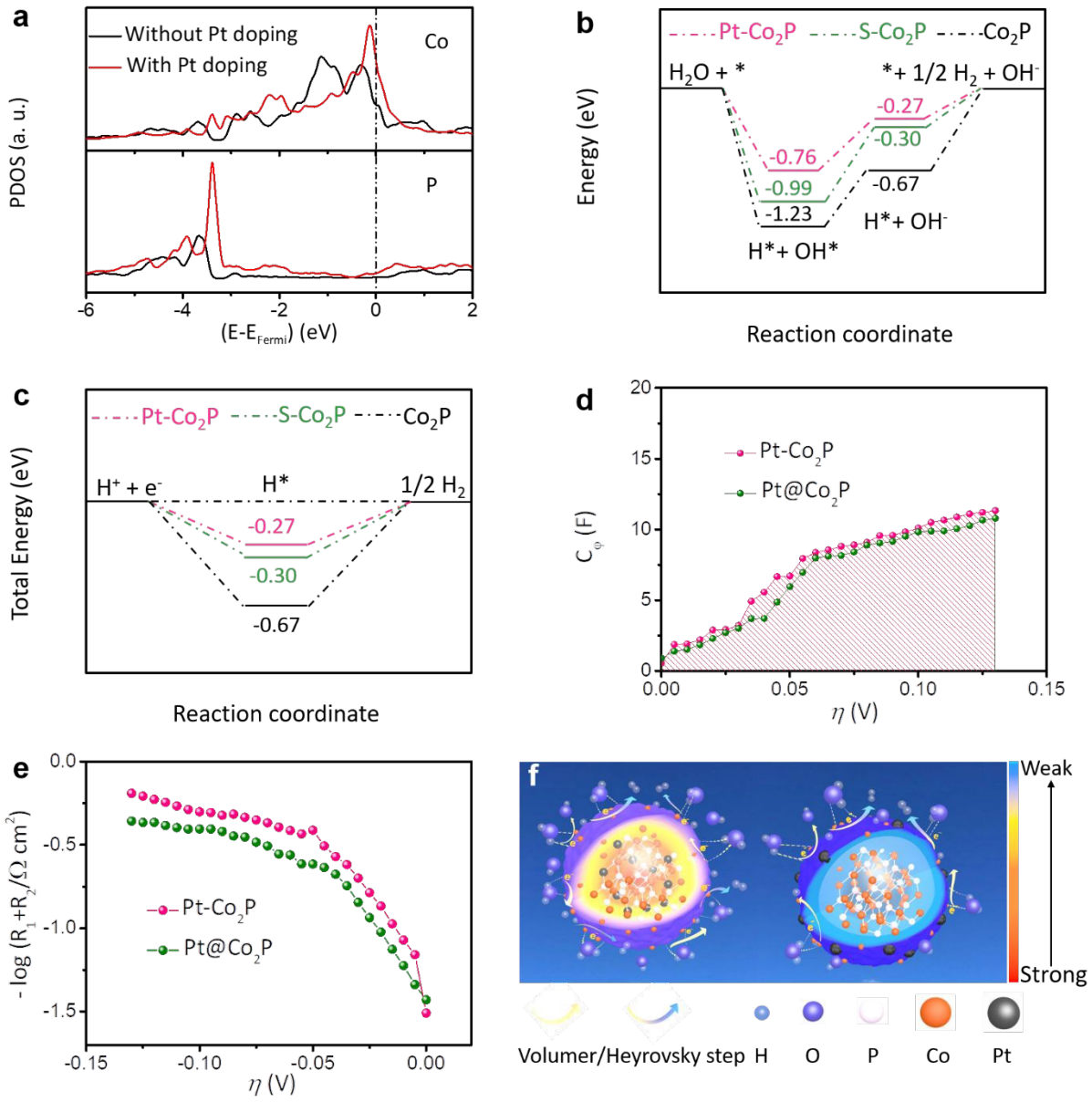

Figure 4. The density of functional theory (DFT) calculations. (a) Partial densities of states (PDOS) for Co and P in the presence and the absence of Pt doping. (b) DFT calculated reaction pathway and (c) calculated H adsorption energies for Pt-Co_2P, S-Co_2P, and Co_2P, respectively. (d) The C_φ-η plot for Pt-Co_2P and Pt@Co_2P. (e) The EIS-Tafel plots. (f) The proposed A-HER mechanism and reaction pathways for Pt-Co_2P (left) and Pt@Co_2P (right). The charge intensity is suggested by the color scale bar. The balls with red, white, black, purple, and transparent colors represent Co, P, Pt, O, and H atoms, respectively.